Equation of state, adiabatic sound speed, and Grüneisen coefficient of boron carbide along the principal Hugoniot to 700 GPa

D. E. Fratanduono,[1,*] P. M. Celliers,[1] D. G. Braun,[1] P. A. Sterne,[1] S. Hamel,[1] A. Shamp,[2] E. Zurek,[2] K. J. Wu,[1] A. E. Lazicki,[1] M. Millot,[1] and G. W. Collins[1]

[1]*Lawrence Livermore National Laboratory, Livermore, California, 94550, USA*

[2]*Department of Chemistry, State University of New York at Buffalo, Buffalo, New York, 14260, USA*

(Received 27 May 2016; revised manuscript received 7 October 2016; published 16 November 2016)

A equation of state (EOS) experimental technique that enables the study of thermodynamic derivatives into the TPa regime is described and applied to boron carbide (B_4C). Data presented here are principal Hugoniot sound speed measurements reported using a laser-driven shock platform, providing a means to explore the high-pressure off-Hugoniot response of opaque materials. The extended B_4C Hugoniot suggests the presence of a high-pressure phase, as recently predicted by molecular dynamics simulations, adding to the complexity of the existing phase diagram.

DOI: 10.1103/PhysRevB.94.184107

I. INTRODUCTION

Boron carbide (B_4C) possesses many unique material properties that warrant its use in a variety of applications. B_4C is the third hardest material after diamond and cubic boron nitride. It is of low density (2.52 g/cc) with high strength [1,2] and has a high melting point (2743 K) [3] and a low wear coefficient [4]. As a result, B_4C is ideal for lightweight armor [5], spacecraft whipple shielding [6], wear-resistant materials, cutting tools, and for use in high-temperature electronic and thermoelectric devices [7–10].

B_4C is a member of the icosahedral boron compounds, a family of crystalline solids with diverse and unique material properties [9,10]. The high strength and low compressibility of B_4C is attributed to the force transfer between the rigid icosahedral structural units. Due to the idealized carbon rich B_4C (or $B_{12}C_3$) stoichiometry, one would presume that boron atoms would be found in the icosahedra and the carbon atoms in the triatomic linker chains. Electronic structure calculations, primarily based upon density functional theory (DFT) [11–18], have shown the most stable atomic arrangement is where one of the boron atoms prefers to be located in the center of the three atom chain, the phase written as $(B_{11}C)CBC$.

Under static compression, the icosahedral units compress less than the bulk of the crystal, retaining their close-to-ideal geometry [10], while under dynamic compression the behavior is more complex [1–3,19–25]. Two polymorphic phase transitions at pressures of 30–50 GPa and ∼50 GPa have been postulated and debated based upon nanoindentation experiments [26–28], Hugoniot data and shock wave profile analysis [2,3,24,25,29]. Nanoindentation experiments [26–28] examined structural damage under contact loading of recovered samples. These experiments found narrow amorphous bands and local disorder areas and evidence for a high-pressure amorphous phase above 40 GPa. Shock wave experiments found anomalous changes in the compressibility and structured shock wave profiles indicative of at least one phase transition at similar pressures. Extrapolation of the low pressure Hugoniot data to pressures >100 GPa conditions suggests a soft material response, limiting the usefulness of B_4C against hypervelocity impacts [30]. In this paper, we extend the dynamic equation of state (EOS) of B_4C to 700 GPa in order to examine the high-pressure behavior. We find a stiffer response than previously predicted, and potential evidence for a high-pressure phase, adding to the complexity of the phase diagram.

The B_4C principal Hugoniot was determined through impedance matching to a quartz reference [31]. Small time-dependent modulations in the drive laser intensity produce similar modulations in the shock front velocity that are observed with a sensitive velocimetry interferometer [32]. We have developed a first-order perturbation analysis [33] that correlates velocity modulations in a reference material (quartz) to those in a sample (B_4C) in order to infer the sound speed and the Grüneisen coefficient [34] in the sample. Here, we present high precision shock Hugoniot EOS measurements, and we apply this technique to determine derivatives of the state variables Eulerian sound speed (C_s) and the Grüneisen coefficient (Γ). These data suggest the presence of a high-pressure phase transition consistent with molecular dynamics simulations [35].

II. EXPERIMENTAL TECHNIQUE

Experiments were conducted at the Laboratory for Laser Energetics (LLE) at the University of Rochester [36]. The inner walls of a gold half-hohlraum were irradiated by 21 beams of the OMEGA laser to produce a uniform x-ray drive onto the mounted sample (see Fig. 1). A composite pulse shape, 6 ns in duration with energy ranging from 1600 to 5600 J, was used to drive a nearly steady shock wave in the B_4C sample.

The targets consisted of an ablator attached to an α-quartz baseplate upon which a hot-pressed B_4C opaque sample and α-quartz witness were also attached (see inset of Fig. 1). A second quartz witness was bonded to the rear surface of the B_4C enabling the shock velocity perturbations to be observed once the shock wave exited the sample. Along the center line of the target, 100 μm region of the quartz baseplate and B_4C sample were left bare to enable transit time measurements.

The average grain size in our B_4C samples, determined with electron backscatter diffraction (EBSD), was found to

*Fratanduono1@llnl.gov

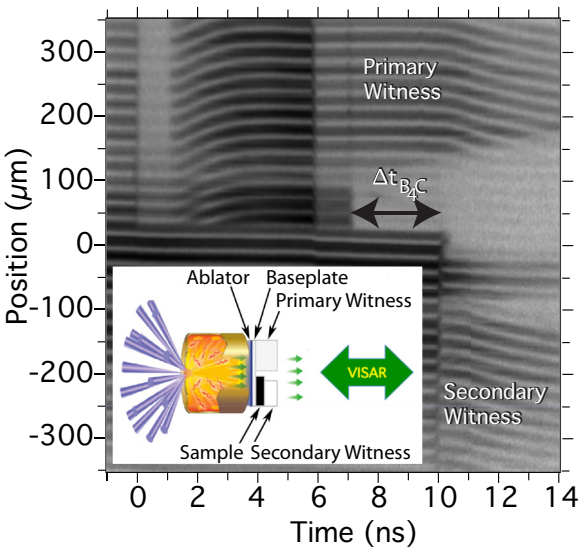

FIG. 1. Raw experimental VISAR data from a low-pressure target design. Inset illustrates the target design. The top half of the target corresponds to the quartz witness and the bottom is the B_4C sample. At ~6 ns, the shock breaks out of the CH ablator, at ~7 ns the shock enters the B_4C, and at 10 ns the shock exits the B_4C and enters the secondary quartz witness.

be 10 μm with random orientation. Measured bulk sample density was 2.51(± 0.01) g/cm^3. X-ray diffraction revealed graphitic inclusions thus reducing the sample density below the full theoretical crystalline density of 2.52 g/cm^3.

Six low-pressure (<500 GPa) and five high-pressure (>500 GPa) experiments were performed. The low-pressure experiments utilized a ~75 μm thick CH ablator, ~16 μm baseplate, and ~46 μm thick sample and the high-pressure experiments utilized a ~54 μm thick Be ablator, ~45 μm baseplate, and ~76 μm thick sample. The B_4C sample thicknesses were measured using a dual confocal microscope, and the glue layer thicknesses were determined by measuring target thickness after assembly. Each sample package was glued over a 1.5 mm hole at one end of the gold half-hohlraum.

The primary quartz witness shock velocity and a secondary quartz witness shock velocity were measured using a line-imaging velocity interferometer system for any reflector (VISAR) [32]. The VISAR diagnostic and a streaked optical pyrometer (SOP) [37] were used to measure the shock transit times of the sample. The VISAR etalon velocity per fringe (VPF) used in camera 1 and 2 were 6.9065 and 2.7318 km/s/fringe, respectively. Fringe positions in the data analysis were resolved to within 3% of the respective VPFs. An example raw VISAR data record is shown in Fig. 1. The temporal resolution of the three streak cameras VISAR A, VISAR B, and SOP were 29 ps, 16 ps, and 17 ps, respectively.

III. ANALYSIS AND RESULTS

A. Nonsteadiness correction

The principal Hugoniot was determined from the measured shock velocity in the B_4C and the quartz baseplate through impedance matching. For opaque materials with steady shock waves, impedance matching to a standard is a well established technique [38]. An unsteady drive can lead to systematic uncertainties when inferring the shock velocity from the transit time in the opaque B_4C sample. We utilize the techniques described by Fratanduono *et al.* [33] to account for the wave unsteadiness.

For quasisteady shock waves with small acoustic perturbations ($\Delta P/P < 10\%$), linear scalings in the time and amplitude relate acoustic modulation signals observed at the shock front to the ablation front. For multisection targets that experience a common source, the modulations propagating through each region are related through linear scaling parameters.

The unsteady wave analysis requires a witness material, quartz in this case, to provide a continuous measurement of the shock velocity modulations over the duration of the measurement. Doppler shifts of the wave speed modulations measured in the quartz primary reference shock velocity are used to infer the corresponding variations of shock velocity within the opaque B_4C sample. This requires accurate knowledge of the principal Hugoniot and release states of quartz throughout the measurement domain. Accurate fits to an extensive database of quartz shock and release data have recently been provided by Knudson and Desjarlais [31,39].

Impedance matching to the quartz baseplate requires an accurate determination of the B_4C shock velocity when the shock first enters the sample. This is determined from the transit time (average velocity) measurements together with a correction to account for velocity variations during the transit. The correction requires the B_4C Hugoniot and the Doppler scaling factor ($F = \Delta t^{quartz}/\Delta t^{B_4C}$). Since these parameters are unknown *a priori*, we begin by using estimated values and iterate to determine each of these quantities (see Secs. III B and III D). Since the correction to the shock velocities are small, convergence is achieved in three iterations.

During transit through the opaque sample, we define the shock velocity as

$$U_s^{B_4C}(t - t_1) = \left\langle U_s^{B_4C} \right\rangle + \delta U_s^{B_4C}(t - t_1), \text{ for } t_1 \leqslant t \leqslant t_2, \tag{1}$$

where $\langle U_s^{B_4C} \rangle$ is the average B_4C shock velocity and $\delta U_s^{B_4C}(t - t_1)$ is the correction accounting for the shock wave unsteadiness [40]; t_1 corresponds to the time the shock enters the sample and t_2 is the time when the shock exits the sample.

The correction ($\delta U_s^{B_4C}$) is determined from the quartz witness measurement. The quartz witness and the B_4C modulations are related by

$$\delta U_s^{B_4C}(t - t_1) = G_{B_4C}\delta U_s^{Qz}\left(\frac{(t - t_1)}{F_{B_4C}}\right) \text{ for } t_1 \leqslant t \leqslant t_2, \tag{2}$$

where the linear scaling Doppler parameter (F_{B_4C}) and the linear scaling amplitude parameter (G_{B_4C}) account for interactions of the perturbation signal with the various (dynamic) features of the target (material interfaces and reflected waves within the target) [33]. The G_{B_4C} parameter requires knowledge of the quartz Grüneisen coefficient. This should not be confused with the parameter Γ_{eff} (*effective* Grüneisen parameter) reported in Knudson and Desjarlais [31]. We extracted the true quartz Grüneisen coefficient by eval-

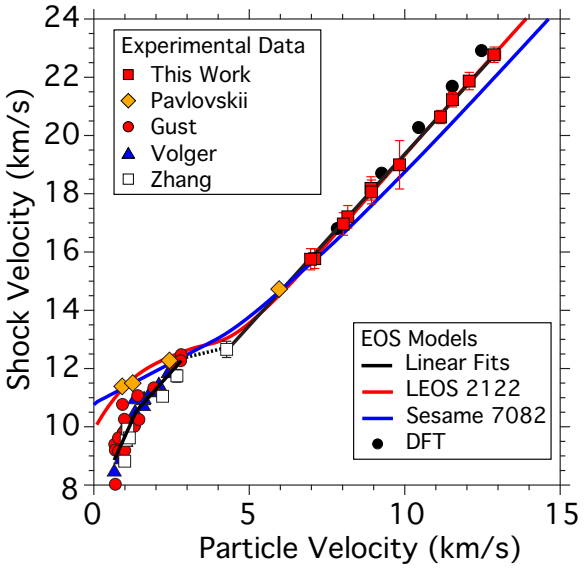

FIG. 2. B_4C shock velocity versus particle velocity. The experimental measurements from this work are shown in red and are compared with previous low pressure experiments (red circles [21], orange diamonds [22], blue triangles [25], and white squares [3]), Sesame table 7082 [41] (blue line), our LEOS (Livermore Equation of State) 2122 model (red line), density-functional theory (DFT) simulations (black points), and linear fits to the experimental data (black solid lines). A plateau in shock velocity (black dashed line) is observed at ~12.5 km/s.

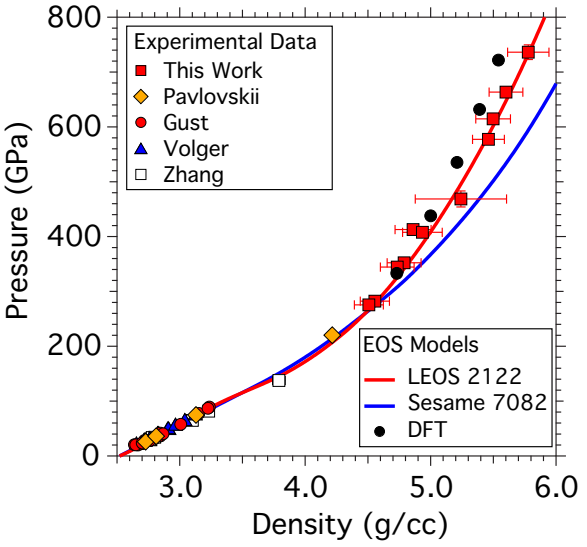

FIG. 3. B_4C Principal Hugoniot pressure versus density. The experimental measurements from this work are shown in red and are compared with previous low pressure experiments (red circles [21], orange diamonds [22], blue triangles [25], and white squares [3]), Sesame table 7082 [41] (blue line), our LEOS 2122 model (red line), and DFT simulations (black points).

uating $\Gamma = VdP/dE|_V$ along the Hugoniot and release isentropes as prescribed by Knudson and Desjarlais.

The quartz shock front perturbation δU_s^{Qz} is defined as

$$\delta U_s^{Qz}(t - t_1) = U_s^{Qz}(t - t_1) - \left\langle U_s^{Qz} \right\rangle, \quad (3)$$

where $U_s^{Qz}(t)$ is the measured quartz shock velocity and $\langle U_s^{Qz} \rangle$ is the average shock velocity in the quartz witness defined as

$$\left\langle U_s^{Qz} \right\rangle = \frac{\int_0^{\frac{\Delta t_{B_4C}}{F_{B_4C}}} U_s^{Qz}(t - t_1)dt}{\frac{\Delta t_{B_4C}}{F_{B_4C}}}. \quad (4)$$

Using the quartz EOS and the *a priori* estimates along the B_4C Hugoniot the linear scaling terms are determined. We can then determine the B_4C shock velocity using Eq. (1).

For these experiments, the correction to the shock velocity was on average 0.10 km/s (~0.5% correction) significantly less than the random uncertainties in the shock velocity. The shock velocity versus particle velocity is shown in Fig. 2, and pressure versus density is shown in Fig. 3. A linear fit to our high-pressure U_s vs u_p gives

$$U_s[\text{km/s}] = 7.36(\pm 0.13)[\text{km/s}] + 1.198(\pm 0.014)u_p[\text{km/s}]. \quad (5)$$

The experimental measurements are summarized in Table I. The experimental errors arise from uncertainty in the sample thickness, the measured transit time of the sample, the measured quartz shock velocity, the unsteady wave correction, and uncertainties associated with the quartz EOS.

A two segment linear fit was performed to the low-pressure ($P < 100$ GPa) B_4C [3,21,25] Hugoniot data. The two line segments represent the data well and are defined by

$$U_s[\text{km/s}] = 7.1(\pm 0.9)[\text{km/s}] + 2.36(\pm 0.4)u_p[\text{km/s}], \quad (6)$$

and

$$U_s[\text{km/s}] = 8.89(\pm 0.6)[\text{km/s}] + 1.2(\pm 0.2)u_p[\text{km/s}]. \quad (7)$$

These fits determine a breakpoint in shock velocity at 10.5(±0.4) km/s consistent with previous fits [2,3]. A linear fit to all available high-pressure ($P > 100$ GPa) Hugoniot data gives

$$U_s[\text{km/s}] = 7.6(\pm 0.3)[\text{km/s}] + 1.18(\pm 0.03)u_p[\text{km/s}]. \quad (8)$$

These fits are shown as the black lines in Fig. 2. A plateau in shock velocity is observed at ~12.5 km/s (black dashed line in Fig. 2), potentially indicative of a high-pressure phase.

B. Lagrangian sound speed determination

The target configuration comprising a quartz primary witness in parallel with secondary witness affixed to the rear of the sample enables one to extract further information through a detailed cross correlation of the perturbation patterns. Each section of the target experiences a common quasisteady pressure source. Modulations in the pressure drive are observed as modulations in the shock front amplitudes and as Doppler shifts in the arrival time. A schematic of this process is shown in Fig. 4. For an opaque sample, the correlation of perturbations between the sample and the witness is unknown since only the transit time (Δt_{sample}) is observed. By attaching a second transparent witness (black trace) to the rear of the sample, the perturbations in the primary witness and the secondary witness can be cross correlated. The signals transmitted through the

TABLE I. Boron carbide Hugoniot measurements.

Shot Number	Thickness μm	U_s^{Quartz} km/s	$\langle U_s^{B_4C}\rangle$ km/s	δU_s^{B4C} km/s	$U_s^{B_4C}$ km/s	P GPa	ρ g/cc	up km/s	F unitless	Cs km/s	Γ unitless
s69619	79.1(±0.5)	19.2(±0.2)	20.6(±0.2)	−0.07	20.6(±0.2)	577(±9)	5.46(±0.13)	11.1(±0.2)	1.07(±0.04)	17.6(±0.9)	0.6(±0.2)
s69618	75.6(±0.5)	19.7(±0.2)	21.2(±0.2)	0.05	21.3(±0.2)	615(±10)	5.50(±0.14)	11.5(±0.2)	1.06(±0.02)	18.2(±1)	0.5(±0.2)
s69617	74.7(±0.5)	21.4(±0.2)	22.8(±0.3)	−0.18	22.6(±0.3)	736(±13)	5.78(±0.17)	12.9(±0.2)	1.00(±0.01)	19.6(±1.2)	0.5(±0.2)
s69616	77.7(±1)	20.4(±0.1)	21.9(±0.3)	−0.12	21.8(±0.3)	663(±8)	5.60(±0.13)	12.1(±0.1)	1.25(±0.02)	16.2(±0.6)	0.9(±0.3)
s69622	46.7(±1)	16.3(±0.1)	18.5(±0.4)	−0.28	18.2(±0.4)	413(±8)	4.86(±0.14)	8.9(±0.1)	1.15(±0.04)	16.8(±0.9)	0.4(±0.3)
s69623	45.9(±1)	15.2(±0.1)	17.2(±0.4)	0.0	17.2(±0.4)	352(±6)	4.79(±0.14)	8.2(±0.1)	1.15(±0.02)	16.0(±0.8)	0.4(±0.4)
s69624	44.6(±1)	15.1(±0.1)	17.1(±0.4)	−0.14	17.0(±0.4)	344(±6)	4.73(±0.13)	8.0(±0.1)	1.19(±0.01)	15.7(±0.8)	0.5(±0.3)
s69625	48.8(±1)	13.8(±0.1)	15.8(±0.3)	−0.06	15.8(±0.3)	282(±5)	4.56(±0.12)	7.1(±0.1)	1.19(±0.02)	15.1(±0.7)	0.3(±0.4)
s69627	46.0(±1)	13.6(±0.1)	15.9(±0.4)	−0.12	15.8(±0.4)	276(±5)	4.51(±0.12)	7.0(±0.1)	1.21(±0.03)	15.0(±0.7)	0.4(±0.3)
s69628	45.1(±1)	16.3(±0.1)	18.2(±0.4)	−0.15	18.1(±0.4)	408(±8)	4.93(±0.16)	8.9(±0.1)	1.15(±0.03)	16.3(±0.9)	0.5(±0.4)
s69621[a]	46.1(±2)	17.4(±0.1)	19.0(±0.8)			469(±15)	5.24(±0.36)	9.8(±0.2)			

[a]No quartz witness for this experiment.

sample into the secondary witness depend on the sound speed and Grüneisen coefficient of the sample. From this analysis, one can determine the relative Doppler shifts of events experienced by the sample and the primary witness ($\Delta t_{\text{Witness}}/\Delta t_{\text{sample}}$). Prior to the shock exiting the sample, the timing of events between the primary witness and sample (for the configuration shown in Fig. 4) is defined as

$$\frac{\Delta t_{\text{Witness}}}{\Delta t_{\text{sample}}} = \frac{1+M_U}{1+M_D}\frac{1}{1-M_{\text{Witness}}}\frac{1-M_{\text{sample}}}{1}, \tag{9}$$

where M_U and M_D are the upstream and downstream Mach numbers of the reshock or release wave at the baseplate/sample interface, M_{Witness} is the downstream Mach number of the shock front in the witness, and M_{Witness} is the downstream Mach number of the shock front in the sample. Provided that the mechanical EOS of the witness and baseplate are known, M_U, M_D, and M_{Witness} are defined. The Mach number within the sample is defined as

$$M_{\text{sample}} = \frac{P}{\rho C_s u_p}, \tag{10}$$

where P is pressure, ρ is the density, u_p is the particle velocity, and C_s is the Eulerian sound speed of the sample defined along the principal Hugoniot.

A nonlinear least squares optimization was used to determine the linear scaling parameters that map the secondary quartz witness shock velocity onto the primary quartz witness shock velocity. Specifically, three parameters were optimized: the Doppler scaling factor ($F = \Delta t^{quartz}/\Delta t^{B_4C}$), the amplitude scaling factor ($G = \Delta u_s^{quartz}/\Delta u_s^{B_4C}$), and $\Delta t_{\text{Witness}}$, a free parameter that relates the primary witness signal to the corresponding (unobserved) signal in the sample. The B_4C sound speed was determined from Eqs. (9) and (10) and the inferred $\Delta t_{\text{Witness}}$. This requires that the transit time of the sample, the principal Hugoniot of the B_4C, and the EOS of quartz are known. The measured B_4C sound speed measurements are provided in Table I and shown in Fig. 5. One assumption, implicit in this technique, is that both the sample and the witness have no strength; we assume that the B_4C is in the liquid state and has no shear strength.

C. Grüneisen coefficient

For small isentropic fluctuations about a shock state, the Grüneisen coefficient can be determined by isentropic expansion of a state on the principal Hugoniot. Along the principal Hugoniot, the Grüneisen coefficient is defined by [34]

$$\Gamma = \frac{2}{\rho}\frac{\rho^2\left(C_s^2 - dP/d\rho|_H\right)}{P - \rho^2\, dP/d\rho|_H(1/\rho_o - 1/\rho)}, \tag{11}$$

where P is the Hugoniot pressure, ρ is the Hugoniot density, ρ_0 is the initial sample density, C_s is the Eulerian sound speed, and $dP/d\rho|_H$ is pressure derivative with respect to density along the Hugoniot.

Utilizing the principal Hugoniot experimental data (see Table I), a linear fit to the U_s-u_p data, and the measured sound speed, the Grüneisen coefficient is determined. The experimental results are provided in Table I and shown in the inset of Fig. 5. These measurements are in agreement with the Sesame 7082 and our LEOS 2122 model which was constructed to fit this data, but are not in agreement with simulations. Our measurements cannot discern between Sesame 7082 and the LEOS 2122 model.

D. EOS models

A new tabular EOS model for B_4C was developed to provide a thermodynamically-consistent representation of the equilibrium EOS. The model uses a global-range approach that extends from the low-temperature solid to high-temperature plasma conditions within a consistent framework [42]. The model used here includes a number of additional features beyond those described in More *et al.* [42], most notably a more flexible representation for the density dependence of the Grüneisen coefficient, and cold-curve break points which can be used to represent the effects of solid-solid phase transitions [43]. This model was fit to diamond anvil cell data [10] as well as the Hugoniot data, sound speeds, and Grüneisen gamma values from this work. This tabular EOS model is now identified as LEOS (Livermore Equation of State) 2122 in the LEOS data library at Lawrence Livermore National Laboratory. The model is shown as the red line in Figs. 2, 3, and 5. A break point was added at a density of 3.1 g/cc, above the highest measured diamond anvil cell data

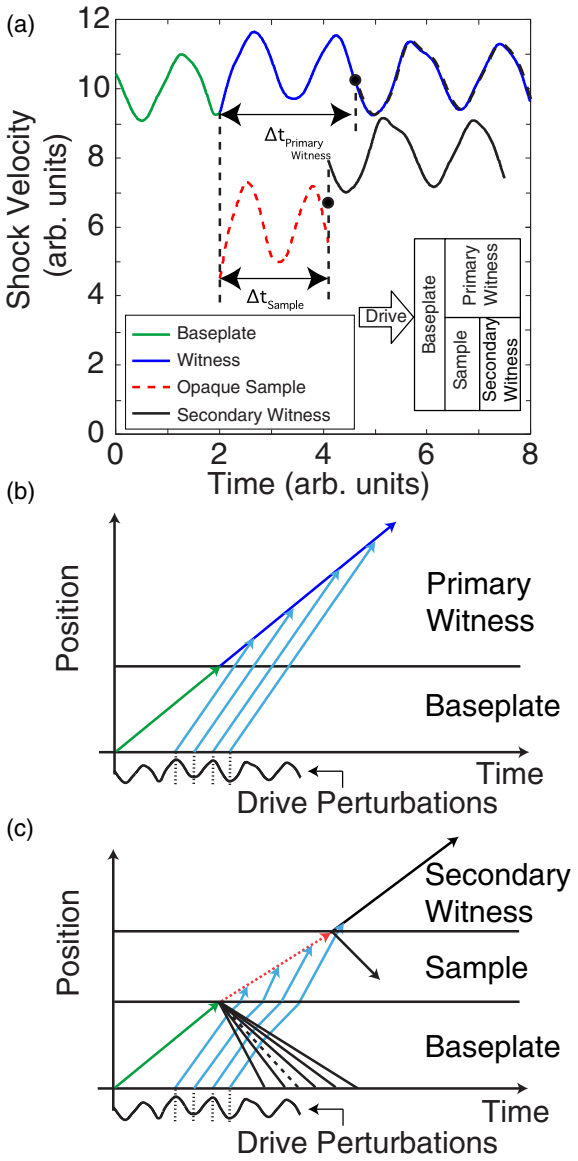

FIG. 4. A schematic of the analysis technique to determine the sound speed of an opaque sample. (a) The shock velocity is tracked in both a primary witness (shown in blue) and a secondary witness (shown in black); the shock velocity history in the sample is not measured (red dashed line). The primary and secondary witness velocities are related over a specific time range through time and amplitude scaling factors. By mapping the secondary witness signal onto the primary witness signal, the common time interval is found defining common events between the opaque sample (Δt_{sample}) and witness ($\Delta t_{\text{Witness}}$). (b) and (c) illustrate the shock front velocity and perturbation originating at the source. Each perturbation (shown in blue) is refracted as it interacts with wavefronts and interfaces.

point [10], in order to fit the higher-pressure Hugoniot data. This density corresponds to a shock velocity of 12.3 km/s along the Hugoniot, in good agreement with the location of the change in the slope in U_s-u_p curve in the data in Fig. 2. The LEOS 2122 model fits all of the high-pressure EOS data well.

Density functional theory based molecular dynamics (DFT-MD) simulations have been carried out to investigate the behavior of boron carbide under shock compression up to 1.5

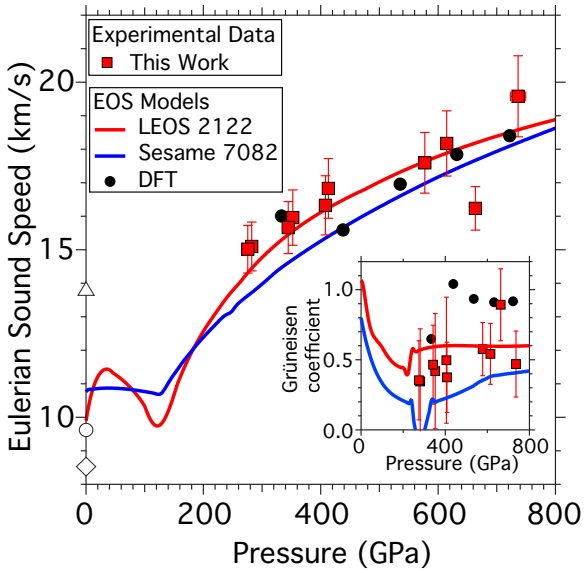

FIG. 5. B_4C Eulerian sound speed vs pressure and inset shows the Grüneisen coefficient vs pressure both determined along the principal Hugoniot (red points). Measurements are compared with Sesame table 7082 (blue line), DFT (black circles), and our LEOS 2122 model (red line) fit to these data. The longitudinal velocity, bulk velocity, and shear velocity at ambient conditions are shown as the white triangle, circle, and diamond, respectively. This analysis assumes that the sample is fluid (has no strength).

TPa using finite-temperature density functional theory [44] (DFT) within the Perdew-Burke-Ernzerhof generalized gradient approximation (PBE-GGA) [45] as implemented in VASP [46,47]. The simulations were carried out in the canonical (NVT) ensemble using Born-Oppenheimer dynamics with a Nose-Hoover thermostat. For each P and T, the system was equilibrated within 1–2 ps and simulated using a 0.75 fs ionic time step. All DFT-MD simulations were carried out with 120-atom supercells, 3- and 4-electron projector augmented wave pseudopotentials [48] with 1.7 and 1.5 Bohr core radii for boron and carbon atoms, respectively, and a 700 eV plane-wave cutoff. For the P-T points closest to the Hugoniot the DFT-MD simulations were repeated with harder pseudopotentials—1.1 Bohr core radii and 900 eV plane-wave cutoff. In the past, theoretical calculations have played an important role in explaining and validating shock-wave measurements [49–56]. A publication describing the computational details, results, and analysis of the DFT-MD data will be published at a later date.

Our experimental results are also compared with the Sesame table 7082 for B_4C [41] (blue line) and DFT simulations (black points) in Figs. 2, 3, and 5. Sesame table 7082 was developed through an additive volume mixture of a boron and diamond EOS for the cold curve, the electronic contribution was calculated using Thomas-Fermi-Dirac, and the thermal nuclear part was determined using a Debye model. We find that this Sesame EOS does not represent our high-pressure Hugoniot data in Fig. 3 well, since the experimental results are stiffer than the model predictions. However, the DFT simulations are in better agreement with the experimental data. The simulations predict a slightly stiffer response than

observed, to within the error bars. The DFT results are also in agreement with the sound speed measurements. The disagreement between the DFT Grüneisen coefficient values and experimental measurements is due to the stiffer response of the Hugoniot predicted by DFT.

The U_s-u_p data shown in Fig. 2 shows that a linear extrapolation of these high-pressure data are consistent with the highest pressure measurements of Zhang *et al.* [3] and Pavlovskii [22], but with a slope significantly larger than in the range $1 < u_p < 5$ km/s, indicating reduced compressibility. This suggests that a high-pressure phase may be forming above ∼130 GPa as predicted by recent molecular dynamics simulations [35] and supported by the good agreement between the EOS model and the higher-pressure Hugoniot data only after the addition of the break point at 3.1 g/cc in LEOS 2122.

One concern regarding the conclusions of a phase based upon the development of the LEOS model is that we have assumed the B_4C is liquid and has no strength. As we have no experimental measure of the shock-melting pressure, the sound-speed measurements may be in error, and conclusions drawn from the modeling could be incorrect. The linear scaling parameters are accurate but their interpretation (extraction of the sound speed) may be in error. Further investigations of B_4C are required to better understand the phase diagram. Independent of the sound speed measurements, the Hugoniot data shows a plateau in shock velocity at ∼12.5 km/s consistent with a phase change.

IV. CONCLUSIONS

The B_4C principal Hugoniot, sound speed, and the Grüneisen coefficient were determined experimentally from ∼250 to ∼700 GPa. We have utilized an analysis technique to correct Hugoniot data for nonsteadiness and to determine the sound speed from modulations in the pressure drive. The sound speed analysis assumes that the sample is a fluid (no strength). Since the shock melting pressure of B_4C has not yet been clearly established experimentally, the sound speed measurements may be in error, and further work is needed to investigate melt. We have developed an equation of state model (LEOS 2122) that fits all available high-pressure Hugoniot data above 100 GPa. The combination of all experimental data shows a plateau in shock velocity at ∼12.5 km/s that may indicate the presence of a high-pressure phase.

ACKNOWLEDGMENTS

This work was performed under the auspices of the U.S. Department of Energy by Lawrence Livermore National Laboratory under Contract No. DE-AC52-07NA27344. A.S. acknowledges financial support from the Department of Energy National Nuclear Security Administration under Award No. DE-NA0002006, and E.V. thanks the Alfred P. Sloan Foundation for a research fellowship (2013–2015).

[1] D. E. Grady, J. Phys. IV (France) **04**, C8 (1994).
[2] D. E. Grady, J. Appl. Phys. **117**, 165904 (2015).
[3] Y. Zhang, T. Mashimo, Y. Uemura, M. Uchino, M. Kodama, K. Shibata, K. Fukuoka, M. Kikuchi, and T. Kobayashi, J. Appl. Phys. **100**, 113536 (2006).
[4] A. Ektarawong, S. I. Simak, L. Hultman, J. Birch, and B. Alling, Phys. Rev. B **90**, 024204 (2014).
[5] S. G. Savio, K. Ramanjaneyulu, V. Madhu, and T. B. Bhat, Int. J. Impact. Eng. **38**, 535 (2011).
[6] L. Shu, M. Edmond, and M. William, Spacecraft interactions with hypervelocity particulate environment, in *38th Aerospace Sciences Meeting and Exhibit*, Aerospace Sciences Meetings (American Institute of Aeronautics and Astronautics, 2000).
[7] A. M. Rajendran and D. J. Grove, Int. J. Impact. Eng. **18**, 611 (1996).
[8] P. S. Branicio, R. K. Kalia, A. Nakano, P. Vashishta, F. Shimojo, and J. P. Rino, J. Mech. Phys. Solids **56**, 1955 (2008).
[9] V. Domnich, S. Reynaud, R. A. Haber, and M. Chhowalla, J. Am. Ceram. Soc. **94**, 3605 (2011).
[10] P. Dera, M. H. Manghnani, A. Hushur, Y. Hu, and S. Tkachev, J. Solid State Chem. **215**, 85 (2014).
[11] D. R. Armstrong, J. Bolland, P. G. Perkins, G. Will, and A. Kirfel, Acta Crystallogr. Sect. B **39**, 324 (1983).
[12] D. M. Bylander, L. Kleinman, and S. Lee, Phys. Rev. B **42**, 1394 (1990).
[13] N. Vast, R. Lazzari, J. M. Besson, S. Baroni, and A. Dal Corso, Comput. Mater. Sci. **17**, 127 (2000).
[14] X. Guo, J. He, Z. Liu, Y. Tian, J. Sun, and H.-T. Wang, Phys. Rev. B **73**, 104115 (2006).
[15] J. E. Saal, S. Shang, and Z.-K. Liu, Appl. Phys. Lett. **91**, 231915 (2007).
[16] S. Aydin and M. Simsek, Phys. Status Solidi B **246**, 62 (2009).
[17] K. Shirai, K. Sakuma, and N. Uemura, Phys. Rev. B **90**, 064109 (2014).
[18] A. Ektarawong, S. I. Simak, L. Hultman, J. Birch, and B. Alling, Phys. Rev. B **92**, 014202 (2015).
[19] M. L. Wilkins, Third progress report of light armor program, Report UCRL-50460 (1968).
[20] R. G. McQueen, S. P. Marsh, J. W. Taylor, J. N. Fritz, and W. J. Carter, *The Equation of State of Solids from Shock Wave Studies*, High-Velocity Wave Phenomena (Academic Press, New York, 1970).
[21] W. H. Gust and E. B. Royce, J. Appl. Phys. **42**, 276 (1971).
[22] M. N. Pavlovskii, Sov. Phys. Solid State **12**, 1736 (1971).
[23] T. J. Holmquist, A. M. Rajendran, D. W. Templeton, and K. D. Bishnoi, TARDEC Technical Report No. 13754, U.S. Army Tank-automotive Research, Development, and Engineering Center (1999).
[24] D. P. Dandekar, Shock Response of Boron Carbide, Aberdeen Proving Ground, MD 21005-5066, Weapons and Materials Research Directorate, Army Research Laboratory (2001).
[25] T. J. Vogler, W. D. Reinhart, and L. C. Chhabildas, J. Appl. Phys. **95**, 4173 (2004).

[26] D. Ge, V. Domnich, T. Juliano, E. A. Stach, and Y. Gogotsi, Acta Mater. **52**, 3921 (2004).
[27] X. Q. Yan, W. J. Li, T. Goto, and M. W. Chen, Appl. Phys. Lett. **88**, 131905 (2006).
[28] K. M. Reddy, P. Liu, A. Hirata, T. Fujita, and M. W. Chen, Nature Commun. **4**, 2483 (2013).
[29] D. E. Grady, Analysis of shock and high-rate data for ceramics: Application to boron carbide and silicon carbide, Report Contract No. DAAE07-01-P-L843, ARA Project No. 0778 (U.S. Army TACOM-TARDEC Emerging Technologies Team, 2002).
[30] S. T. Lai, E. Murad, and W. J. McNeil, J. Spacecr. Rockets **39**, 106 (2002).
[31] M. D. Knudson and M. P. Desjarlais, Phys. Rev. B **88**, 184107 (2013).
[32] P. M. Celliers, D. K. Bradley, G. W. Collins, D. G. Hicks, T. R. Boehly, and W. J. Armstrong, Rev. Sci. Instrum. **75**, 4916 (2004).
[33] D. E. Fratanduono, D. H. Munro, P. M. Celliers, and G. W. Collins, J. Appl. Phys. **116**, 033517 (2014).
[34] R. G. McQueen, S. P. Marsh, and J. N. Fritz, J. Geophys. Res. **72**, 4999 (1967).
[35] X. Q. Yan, Z. Tang, L. Zhang, J. J. Guo, C. Q. Jin, Y. Zhang, T. Goto, J. W. McCauley, and M. W. Chen, Phys. Rev. Lett. **102**, 075505 (2009).
[36] T. R. Boehly, R. S. Craxton, T. H. Hinterman, J. H. Kelly, T. J. Kessler, S. A. Kumpan, S. A. Letzring, R. L. McCrory, S. F. B. Morse, W. Seka, S. Skupsky, J. M. Soures, and C. P. Verdon, Rev. Sci. Instrum. **66**, 508 (1995).
[37] J. E. Miller, T. R. Boehly, A. Melchior, D. D. Meyerhofer, P. M. Celliers, J. H. Eggert, D. G. Hicks, C. M. Sorce, J. A. Oertel, and P. M. Emmel, Rev. Sci. Instrum. **78**, 034903 (2007).
[38] Y. Zel'dovich and Y. Raizer, *Physics of Shock Waves and High-temperature Hydrodynamic Phenomena* (DOVER PUBN Incorporated, New York, 2002).
[39] It is important to note that the B_4C and quartz Hugoniot cross in these experiments. The work of Knudson and Desjarlais [31] did not calibrate reshock quartz. Since B_4C and quartz are well impedance matched, we used an extrapolation of the quartz release model parameters to estimate the quartz reshock conditions.
[40] $\delta U_s^{B_4C}(t - t_1)$ is zero for steady wave experiments (i.e., gas-gun experiments).
[41] S. Crockett, Creating new equations of state for high strength materials (boron and boron carbide), Report (Los Alamos National Laboratory, 2006).
[42] R. M. More, K. H. Warren, D. A. Young, and G. B. Zimmerman, Phys. Fluids **31**, 3059 (1988).
[43] D. A. Young and E. M. Corey, J. Appl. Phys. **78**, 3748 (1995).
[44] W. Kohn and L. J. Sham, Phys. Rev. **140**, A1133 (1965).
[45] J. P. Perdew, K. Burke, and M. Ernzerhof, Phys. Rev. Lett. **77**, 3865 (1996).
[46] G. Kresse and J. Hafner, Phys. Rev. B **47**, 558 (1993).
[47] G. E. Kresse and J. Hafner, Phys. Rev. B **49**, 14251 (1994).
[48] P. E. Blöchl, Phys. Rev. B **50**, 17953 (1994).
[49] B. Boates, S. Hamel, E. Schwegler, and S. A. Bonev, J. Chem. Phys. **134**, 064504 (2011).
[50] Y. Zhang, C. Wang, F. Zheng, and P. Zhang, J. Appl. Phys. **112**, 033501 (2012).
[51] Y. Zhang, C. Wang, and P. Zhang, Phys. Plasmas **19**, 112701 (2012).
[52] Y. Zhang, C. Wang, D. Li, and P. Zhang, J. Chem. Phys. **135**, 064501 (2011).
[53] S. Root, K. R. Cochrane, J. H. Carpenter, and T. R. Mattsson, Phys. Rev. B **87**, 224102 (2013).
[54] R. J. Magyar, S. Root, and T. R. Mattsson, JPCS **500**, 162004 (2014).
[55] T. R. Mattsson, S. Root, A. E. Mattsson, L. Shulenburger, R. J. Magyar, and D. G. Flicker, Phys. Rev. B **90**, 184105 (2014).
[56] D. Li, P. Zhang, and J. Yan, J. Chem. Phys. **139**, 134505 (2013).